Journal of Magnetic Resonance 307 (2019) 106567

Contents lists available at ScienceDirect

Journal of Magnetic Resonance

journal homepage: www.elsevier.com/locate/jmr

Enhancing surface coil sensitive volume with hybridized electric dipoles at 17.2 T

Marc Dubois [a,b], Tania S. Vergara Gomez [a,b], Camille Jouvaud [c,d], Abdelwaheb Ourir [e], Julien de Rosny [e], Frank Kober [b], Redha Abdeddaim [a,*], Stefan Enoch [a], Luisa Ciobanu [f]

[a] Aix Marseille Univ, CNRS, Centrale Marseille, Institut Fresnel, Marseille, France
[b] Aix Marseille Univ, CNRS, CRMBM, Marseille, France
[c] CEA-LETI MINATECH, Grenoble, France
[d] Université Grenoble Alpes, Grenoble, France
[e] ESPCI Paris, PSL Research University, CNRS, Institut Langevin, Paris, France
[f] CEA, DRF, JOLIOT, NeuroSpin, UNIRS, Université Paris-Saclay, Gif-sur-Yvette, France

ARTICLE INFO

Article history:
Received 15 February 2019
Revised 1 August 2019
Accepted 5 August 2019
Available online 16 August 2019

Keywords:
High field MRI
Metamaterial
Hybridization
RF shimming

ABSTRACT

Preclinical MR applications at 17.2 T can require field of views on the order of a few square centimeters. This is a challenging task as the proton Larmor frequency reaches 730 MHz. Most of the protocols at such frequencies are performed with surface transceiver coils for which the sensitive volume and the signal to noise ratio (SNR) is given by their size. Here we propose an approach based on metamaterials in order to enhance the sensitive volume of a commercial surface coil for small animal imaging at 17.2 T. We designed a passive resonator composed of four hybridized electric dipoles placed onto the floor of the MRI bed. Combining numerical and experimental results on a phantom and *in vivo*, we demonstrate a 20% increase of the sensitive volume in depth and 25% along the rostro-caudal axis while maintaining more than 85% of the local SNR right beneath the surface coil plane. Moreover, our solution gives the ability to double the average SNR in the region between 1.2 and 2 cm away from the loop using a single layer of 1 mm thick metallic wires easy to design and manufacture.
© 2019 The Authors. Published by Elsevier Inc. This is an open access article under the CC BY license (http://creativecommons.org/licenses/by/4.0/).

1. Introduction

As higher static magnetic field strength keeps on enhancing the signal to noise ratio (SNR) for magnetic resonance applications, it requires a proportional increase in the working frequency of the radio frequency (RF) coils. As an example, a 17.2 T preclinical scanner sets the proton Larmor frequency to 730 MHz. Typical preclinical MR applications can require field of views (FOVs) on the order of a few square centimeters. Homogeneous RF excitation (B_1) covering such FOVs is hard to obtain since RF coil dimensions become comparable with the electromagnetic wavelength. At 730 MHz, the classical volume coil design, like the birdcage coil [1], becomes more sensitive to the nature, size and position of the load [2]. Due to the high operation frequency, smaller capacitance values are required to tune the coil. Consequently, the stray capacitances from the load impact strongly the coil tuning as well as the symmetry of the currents. Moreover, subjects with sections of a few centimeters presenting high relative permittivity already lead to B_1 inhomogeneities because of wavelength reduction. Consequently, surface transceiver coils are commonly used for magnetic resonance imaging (MRI) as well as magnetic resonance spectroscopy (MRS) at extreme B_0 magnitude. As opposed to the volume coils, surface coils can avoid B_1 inhomogeneities arising from dielectric effects or RF interference because the subject is excited unilaterally. However, given their geometry, the magnitude of the B_1 field produced along the main axis decays away from the loop plane as

$$B_1(d) = \frac{\mu_0 I R^2}{2(R^2 + d^2)^{3/2}} \tag{1}$$

with R the radius of the loop, I the current magnitude and d the distance from the loop plane [3]. Although this equation only describes the magnetostatic field which is inaccurate at such frequencies, it illustrates the trade-off between the local sensitivity as $B_1(0) \propto R^{-1}$ and the in depth sensitivity as $B_1(R) \approx B_1(0)/3$. As consequence, a smaller loop would increase the magnetic field amplitude near the loop plane at the cost of a faster magnetic field decay in depth. The RF excitation strategy can be leveraged to solve

* Corresponding author at: Institut Fresnel, 13013 Marseille, France.
E-mail address: redha.abdeddaim@fresnel.fr (R. Abdeddaim).

https://doi.org/10.1016/j.jmr.2019.106567
1090-7807/© 2019 The Authors. Published by Elsevier Inc.
This is an open access article under the CC BY license (http://creativecommons.org/licenses/by/4.0/).

this issue. Adiabatic pulses have been implemented to lower the effect of surface coil sensitivity decay [4,5]. A variety of post-processing methods are also used to compensate this effect [6]. Other approaches, focused on hardware developments, proposed novel surface coil designs in order to benefit from extra degrees of freedom. For example, a dual coaxial ring coil with opposite phase currents was designed to lower B_1 inhomogeneities [7]. Recent work proposed to use a remote patch antenna, similar to traveling wave imaging [8], to image rat brains at 16.2 T [2].

The concept of passive RF shimming was also applied to the improvement of RF coil performances [9]. This strategy consists in placing inductively powered structures close to the loop and/or the object to add secondary sources of B_1 field. Such passive structures can be designed from high relative permittivity dielectric pads exploiting the displacement current within low loss dielectric materials [10,11] or passive conducting loops loaded by lumped elements [7,12,13]. High quality factor composite resonators have also been explored to enhance local sensitivity in ultra-high field MRI (9.4 T) [14,15]. Metamaterials and metasurfaces have emerged as potential candidates to provide flexibility in the surface coil design. Examples of such structures are numerous including hybridized meta-atoms [16,17], fractal metasurfaces [18], and capacitively loaded array of wires [19,20].

In this work, we aimed to develop a hybridized meta-atom (HMA) structure that could easily fit onto the MRI bed without loss of space for preclinical research equipment. The magnetic response of the HMA, used here for passive RF shimming of the surface coil, originates from the electromagnetic coupling occurring due to near field interactions between the four electric dipoles. This particular coupling effect (i.e. generation of magnetic response from electric dipoles) is named hybridization [21] in analogy with bonding and antibonding energies in molecular orbitals [22]. The inductive coupling of the HMA to a commercial surface coil would also guarantee some flexibility in regards to tuning and matching depending on the load and would reduce the design complexity. This specific aspect connects with recent work dedicated to the study of non-resonant coupled-wire structures at lower field strength [17,16,23]. Exploring this concept at extreme B_0 strength (2.5 times higher) represents a new challenge. As the resonator dimensions become comparable with the object under investigation, the loading from the object is stronger and a better filling factor is achieved than in previous realizations at 7 T. Moreover, the distances between the wires and the surface coil correspond to the radiative near field region due to the wavelength reduction in the load.

Here, we designed and built a hybridized meta-atom with four wires surrounding the bottom half of a 2.5 cm diameter cylinder corresponding to the volume of interest for rat brain imaging. The structure was studied numerically and experimentally on a 17.2 T preclinical MRI scanner and compared with a birdcage coil and the original surface coil performances. Finally, we explored the benefits of this structure for *in vivo* rat brain imaging.

2. Methods

2.1. Electromagnetic simulations

Electromagnetic simulations were performed in CST Microwave Studio 2017 (Computer Simulation Technology GmbH, Darmstadt, Germany). The CST time domain solver was used for all simulations with an excitation pulse of 35 ns duration (120 MHz bandwidth) centered on 730 MHz (proton Larmor frequency at 17.2 T). The phantom was designed as a 25 mm diameter cylinder of length 100 mm, with relative permittivity $\epsilon = 60$ and conductivity $\sigma = 0.8$ S/m. A surface coil was placed 1.5 mm above the top of the phantom and four square rods of 90 mm length, 1 mm side, were placed around the phantom at a distance of 3 mm as shown in Fig. 1. All metallic parts were modelled as copper. L-type matching circuits (series and parallel capacitors) were used to tune and match the coil at 730 MHz with and without the HMA. B_1^+ fields, normalized to 1 W accepted power, were extracted at 730 MHz.

2.2. Coil assembling and characterization

Four circular brass rods of 1 mm diameter and 90 mm length were placed onto the small animal bed as in Fig. 2a and b. As we used shorter wire to avoid strong detuning of the loop coil, we also needed to place them away from the loop coil plane. The solution tried was to equally space four wires around a cylinder of 2.5 cm-diameter which represents the floor of the MRI bed used in experiments. There is a tradeoff between the coupling to the surface coil which induces the current in the wires and the spacing between the wires which determines the resulting magnetic field amplitude from such currents. Our strategy consisted on symmetrically placing the wires around the object to image in order to maximize the homogeneity of B_1^+ field inside and avoid the unbalancing of the surface coil. A phantom tube of 25 mm diameter and 50 mm long, containing NaCl solution (3.6 g/L) doped with $CuSO_4$ (1 g/L) was used to characterize the coil with and without the HMA. A commercial 3 cm diameter surface coil (Bruker BioSpin, Ettlingen, Germany) was placed on top of the phantom. The coil tuning and matching were optimized in each case to 730 MHz. On-bench measurements of S_{11} parameters were performed over a 100 MHz bandwidth with a vector network analyser (Rohde & Schwarz GmbH & Co KG, Munich, Germany).

2.3. MRI experiments on phantom

MRI experiments were performed on a horizontal bore animal scanner operating at 17.2 T (Bruker BioSpin, Ettlingen, Germany) equipped with a triaxial gradient system with maximum strength of 1 T/m. For every tested configuration, a FLASH localizer sequence was used after wobble checking, iterative shimming, frequency adjustment and power calibration. A transmit/receive 4.5 cm inner diameter single channel birdcage coil (Rapid Biomedical GmbH, Rimpar, Germany) was used for phantom measurements comparison.

B_1^+ measurements were obtained with an Actual Flip Angle Imaging (AFI) sequence [24–26] with TE = 2.012 ms, TR_1 = 20 ms, TR_2 = 100 ms, FA = 60°. Three orientations were acquired for each configuration with a matrix of $128 \times 128 \times 8$, FOV = 6×6 cm^2 and a total scan time of 2 min 2 s. The axial slice package spanned over 6 cm while sagittal and coronal slice packages spanned over 3 cm.

SNR maps were computed from 2D Multi-slice-multi-echo sequence (SE) with an effective echo time of 7 ms. Sagittal oriented images were obtained with a matrix of $256 \times 200 \times 9$, FOV = 6.4×5 cm^2, slice thickness = 2 mm and inter-slice gap = 0.3 mm, using a TR = 1500 ms which resulted in total scan time of 5 min. The SNR was computed by dividing the magnitude of the signal to the standard deviation of the noise amplitude taken in a region of interest (ROI) located outside of the phantom [27]. Rician noise correction was not applied to the noise value [28] as we studied relative SNR improvement due to the presence of the HMA. Extra care was taken to avoid artifacts across the noise ROI.

2.4. In vivo MRI experiments

In vivo measurements were performed on one rat (Spra- gue Dawley male, Janvier Labs, Saint Berthevin, France). The animal was anesthetized with 3% isoflurane in an induction chamber

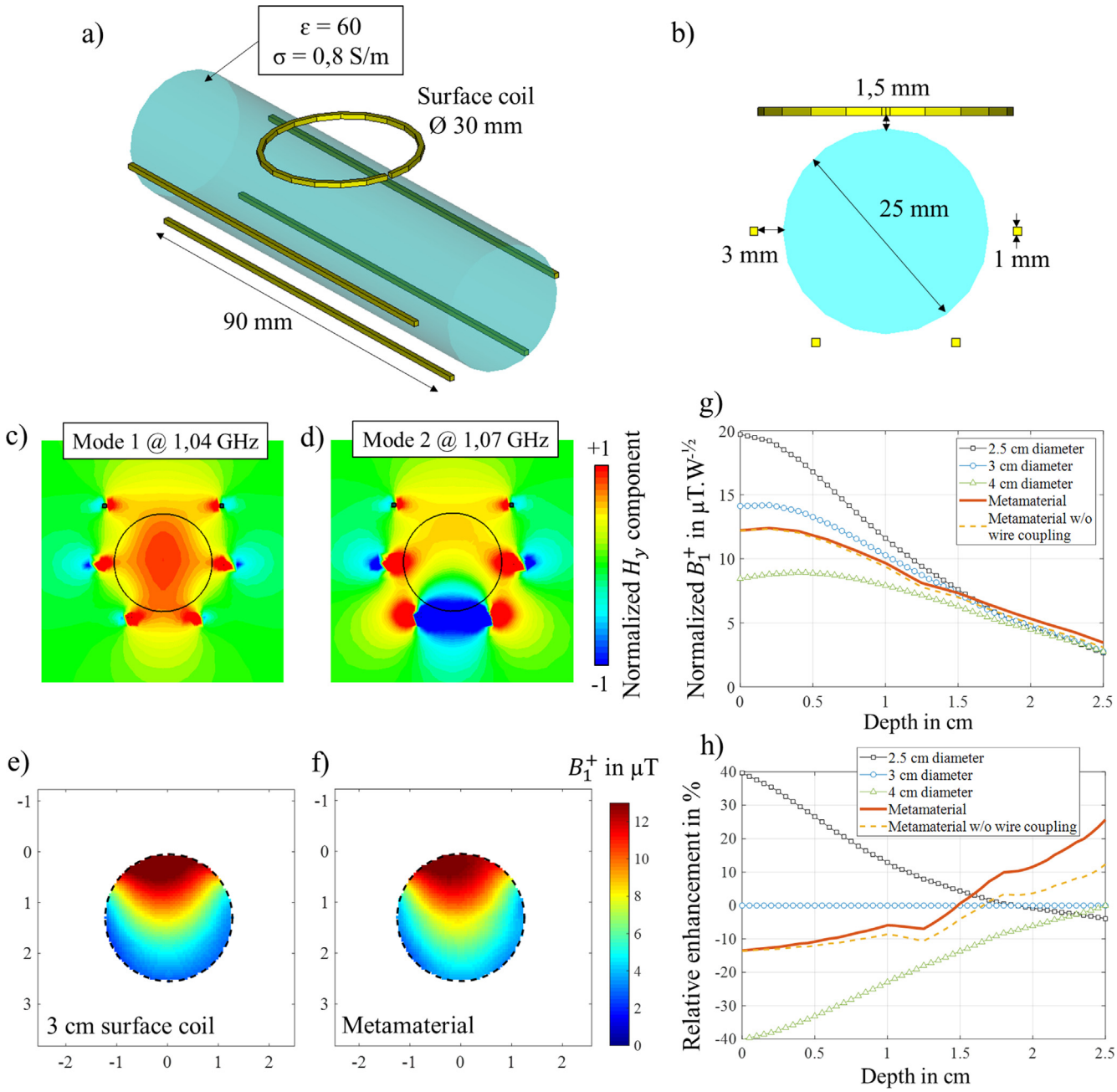

Fig. 1. (a and b) Schematic views of the HMA model used for simulations. Copper (yellow) is used for all metallic parts. We modeled the electromagnetic phantom (blue) as a cylinder of radius 25 mm and length 100 mm. A discrete port (not shown) is placed on the loop for excitation. (c and d) Real part of the H_y magnetic field component in the median axial slice for the two eigenmodes of the HMA. (e) B_1^+ amplitude obtained in the phantom with the loop alone at 730 MHz. Axial slice taken in the center of the phantom with 1 W accepted power. The black dashed circle denotes the phantom location. Relative positions are in cm. (f) B_1^+ amplitude obtained with the HMA added to the loop at 730 MHz. (g) B_1^+ efficiency profile (B_1^+ amplitude normalized to the square root of the input power) in the phantom as function of the depth for the HMA added to the 3 cm loop (solid red) and three loops alone with different diameters: 2.5 cm (black squares), 3 cm (blue circles) and 4 cm (green triangles). The yellow dashed line presents the results of the HMA when the coupling between the wires is artificially removed. (g) Relative enhancement of B_1^+ amplitude as function of depth expressed as percentage. The reference is the 3 cm diameter surface coil without HMA (blue circle). Data are obtained at a frequency of 730 MHz for an accepted power of 1 W. (For interpretation of the references to colour in this figure legend, the reader is referred to the web version of this article.)

and held under anesthesia using 1.5–1.7% isoflurane in a stream of medical air administered through a nose cone. For imaging the rat was placed in prone position head first with the coil placed on top of the brain region. During the MRI exam the respiration rate and body temperature were monitored. The body temperature was maintained between 36.5 and 37 °C using heated water (Grant TC120, Grant Instruments, Shepreth, UK).

All animal procedures used in the present study were approved by the *Comité d'Ethique en Expérimentation Animale, Commissariat l'Energie Atomique et aux Energies Alternatives, Direction des Sciences du Vivant (Fontenay aux Roses, France)* and by the *Ministre de l'Education Nationale de l'Enseignement Supérieur de la Recherche (France)* under reference *APAFIS#2393201510221144753 9v2* and were conducted in strict accordance with the recommendations and guidelines of the *European Union (Directive 2010/63/EU)* and the *French National Committee (Décret 2013-118)*.

Sagittal images were obtained with a 2D RARE (rapid acquisition with relaxation enhancement) sequence with a rare

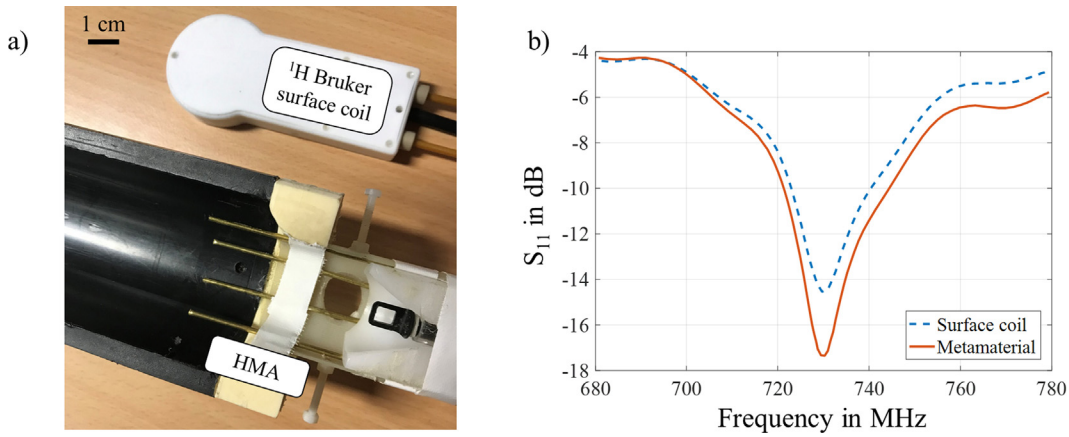

Fig. 2. (a) Photograph of the Bruker surface coil and of the HMA directly positioned onto the animal bed. (b) S_{11} parameter measured with the phantom for the surface coil alone (dashed blue) and in presence of the HMA (solid red). (For interpretation of the references to colour in this figure legend, the reader is referred to the web version of this article.)

factor of 4, TE = 13 ms, TE_{eff} = 26 ms, TR = 5000 ms, matrix of 300 × 150 × 10, FOV = 6 × 3 cm^2, slice thickness = 0.5 mm, inter-slice gap = 1 mm and a total scan time of 1 min 36 s. Axial images were also obtained with a 2D RARE sequence with a rare factor of 4, TE = 11.65 ms, TE_{eff} = 23.3 ms, TR = 3000 ms, matrix of 128 × 128 × 10, FOV = 2.4 × 2.4 cm^2, slice thickness = 1 mm, inter-slice gap = 0.2 mm and a total scan time of 3 min 5 s.

3. Results

Electromagnetic simulation results for the 3 cm diameter loop with and without the HMA are shown in Fig. 1. For 90 mm long wires, we observe a relatively small phase offset (20°) between the HMA rods and the loop currents which means that the current distribution within the HMA respects the symmetry imposed by the loop geometry. This observation is supported by the B_1^+ amplitude maps presented in Fig. 1c and d where we show that the B_1^+ field distribution is not strongly distorted by the presence of the HMA. Nonetheless, one can appreciate an increase in terms of B_1^+ field in depth. This is also confirmed quantitatively by the field profile shown in Fig. 1g. The B_1^+ efficiency (normalized by the square root of input power) obtained with the HMA is better than the loop alone for depths larger than 1.5 cm from the top of the phantom. Moreover, we simulated the B_1^+ efficiencies for loops of diameters 2.5 cm and 4 cm (without HMAs) and results show that the HMA together with a 3 cm diameter loop yields the best performance in the lower part of the phantom. Finally, we used numerical simulations to demonstrate the effect of the mutual interaction or hybridization between the wires. We investigated the different contributions of the currents induced on the wires. These contributions can be separated in two paths, the coupling to the surface coil and the coupling between the wires. Simulating the coupling of the surface coil with each single wire allowed us to separate these two contributions from the original simulation. As a result, it was possible to obtain the B_1^+ efficiency distribution while artificially removing the interaction between the wires shown in Fig. 1g and h. We observed that the hybridization mechanism helped to induce stronger currents in the wires such that higher B_1^+ efficiency can be found. As shown in Fig. 1h, the strongest enhancement at 2.5 cm depth goes from 12% to 25% due to coupling between the wires. It was naturally found in the deepest part of the phantom where the contribution from the surface coil is the lowest due to the decay of magnetic field. More information regarding the currents magnitude and the wires hybridization can be found in supplementary materials section.

Fig. 2a presents a photograph of the commercial coil used and of the assembled HMA. Fig. 2b presents the S_{11} parameter measured with and without the HMA (phantom load in each case). These curves are obtained after optimizing the tuning and matching of the resonance to 730 MHz with the adjustable lumped elements provided with the commercial surface coil. We observe that the presence of the HMA helps reach a better matching of the surface coil. The quality factor of the loop loaded by the phantom is 66 and reaches 88 (+33%) when the HMA is added.

Measured B_1^+ amplitudes in sagittal and axial slices are presented in Fig. 3 for the birdcage coil (a), the 3 cm diameter surface coil alone (b) and in the presence of the HMA (c). The measurements were obtained after a power calibration procedure. Consequently, the three configurations tested show a similar maximum amplitude of about 15 μT. As expected, the birdcage coil provides a better B_1^+ homogeneity than both surface coil configurations. However, the reduction of the wavelength can already be observed across the 2.5 cm diameter phantom. Meanwhile, the presence of the HMA is beneficial for the performance of the surface coil. We observe higher values of the B_1^+ amplitude in depth as expected from the simulation results. The sagittal slices also demonstrate some gain along the long axis of the phantom.

The reference power values obtained were 534 mW, 88 mW and 89 mW for the birdcage coil, the surface coil alone and with the HMA, respectively. The transmission efficiency of the coil can be characterized by the B_1^+ profile as function of depth normalized by the square-root of the reference power which is presented in Fig. 4a. We also present these results in terms of relative improvement with respect to the surface coil alone in Fig. 4b. These results confirm the benefits of adding the HMA to the surface coil leading to 30% higher efficiency between 2 and 2.5 cm away from the loop and a better homogeneity as a smaller difference is observed between the maximum and minimum efficiency values.

We present the *in vitro* SNR results in Fig. 5. The noise value was obtained by calculating the standard deviation in a box of 20 × 20 points in the top left corner of the entire slice package for each configuration. In arbitrary units, these values are 4.7×10^{-6}, 2.5×10^{-6} and 2.2×10^{-6} for the birdcage coil, the surface coil alone and with the HMA, respectively. SNR maps are obtained by dividing the signal maps with the corresponding noise value. Fig. 5c clearly shows the enhancement of the sensitive volume obtained once the HMA is added. The in-depth profile (Fig. 5d) demonstrates a slower decay of the SNR across the phantom. We

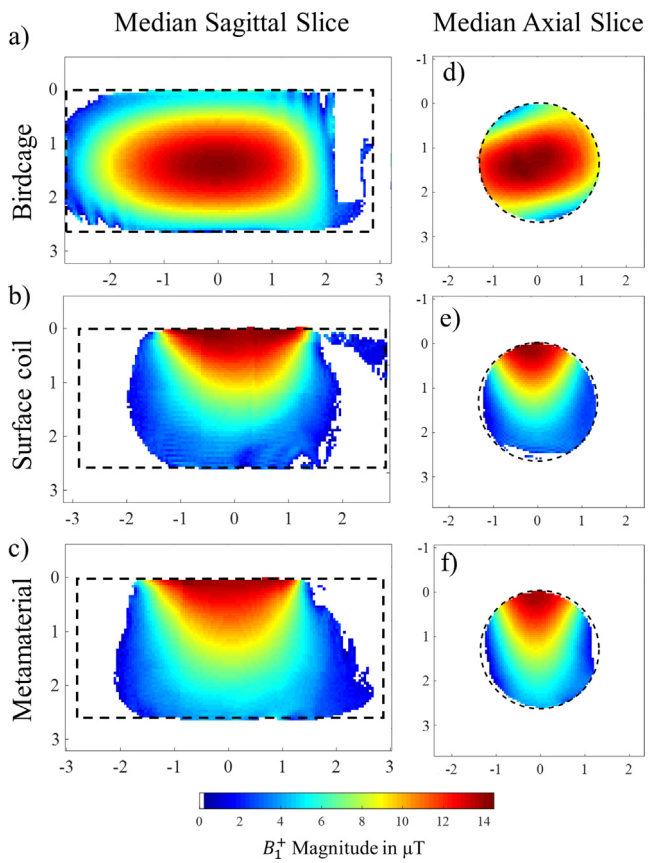

Fig. 3. Measured B_1^+ amplitude in the median sagittal slice with (a) the birdcage coil, (b) the surface coil alone and (c) the surface coil with the HMA. Black dashed boxes denote the position of the phantom. (d–f) B_1^+ amplitude in the median axial slice, respectively. Relative positions are in cm. Measurements are performed after a power calibration procedure.

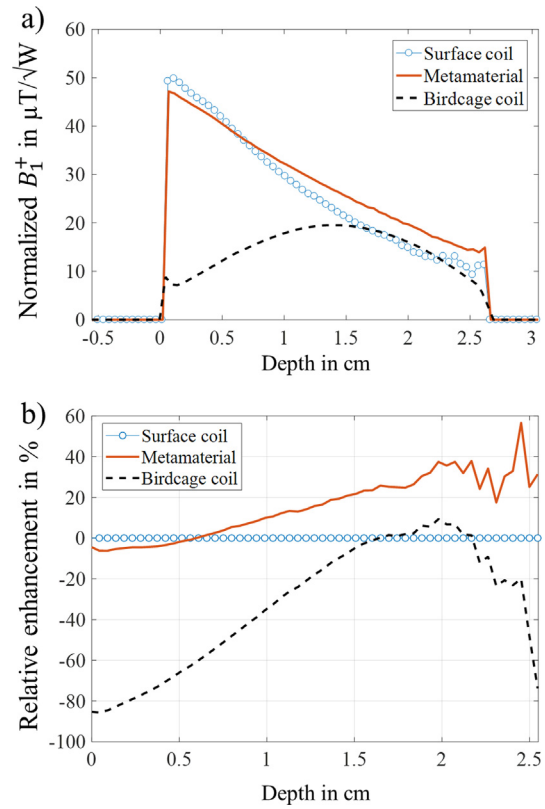

Fig. 4. (a) Measured B_1^+ efficiency profile in function of depth (normalized by the square root of the reference power) for the surface coil alone (blue circles), in presence of the HMA (solid red line) and for the birdcage coil (dashed black line) (b) Relative enhancement of B_1^+ efficiency as function of depth expressed as percentage. The reference is the surface coil without HMA (blue circle). (For interpretation of the references to colour in this figure legend, the reader is referred to the web version of this article.)

observe an increase of the sensitive volume with a full width at half maximum (FWHM) of 1.5 cm (+25%) instead of 1.2 cm for the surface coil alone while the maximum value close to the loop position remains as high as 85 % of the original value in absence of HMA. Moreover, the lateral profile, presented in Fig. 5e, shows an increase of the width of the sensitive volume (FWHM) of 20%.

Finally, we compare the signal maps obtained *in vivo* for the surface coil alone (Fig. 6c) and in presence of the HMA (Fig. 6b and d). We acknowledge a small shift in the positioning of the loop which is set 5 mm toward the left of the image in Fig. 6b compared to Fig. 6a. It is to be noted that the noise values were almost identical for the two configurations in the *in vivo* scans (less than 1% difference). Therefore, it is meaningful to directly compare the signals obtained from each configuration. As expected from the phantom study, the *in vivo* images demonstrate an enlargement of the sensitive volume of the surface coil in depth and along the rostro-caudal direction while observing a slight reduction of signal coming from the top of the brain area which is the region in contact with the loop. From the axial images shown in Fig. 6c and d, we observe a twofold increase of the average signal in the ROI below the brain area. *In vivo* scans with the birdcage coil could not be performed as the bed and the animal equipment would not fit within the inner diameter.

4. Discussion and conclusion

One important aspect for the HMA design is the length of the wires used. Numerical calculations show that the HMA presents its first self-resonance frequency at 1040 MHz as shown in Fig. 1c for 90 mm long wires. In that case, the structure (surface coil & HMA) is tuned and matched to the Larmor frequency (730 MHz) by the lumped capacitors at the surface coil. One could choose a longer wire length to decrease the HMA self-resonance frequency. This length should be close to 200 mm for a frequency of 730 MHz, which corresponds to the half-wavelength resonance condition [16,17]. Due to the presence of the dielectric load close to the wires, the length required is 160 mm in order to set the first self-resonance of the HMA to be at the Larmor frequency in numerical simulation. Such structure may provide a more homogeneous B_1^+ distribution (Fig. 1c) as the current magnitude in the wires will increase but it would require strong changes in the matching network topology of the loop coil used for inductive coupling. Such changes preclude the use of the commercial surface coil available and thus, did not fit our initial requirements. The modification of the matching network topology has already been observed and discussed with metallic resonators [23] and other passive shimming elements like high permittivity dielectric pads [29]. The solution is to set the resonance of the passive element to a higher frequency in order to mitigate the detuning of the active part of the coil. We showed that by reducing the wire length to 90 mm, we were able to modify the B_1^+ distribution of the surface coil without a strong impact on the matching circuit values. Numerical results showed that the presence of the HMA required a reduction of 4% of the series capacitance and of 40% for the parallel one in the surface coil matching circuit. As shown in Fig. 2b, the tuning range of the commercial coil was able to comply with such changes. Additional simulation results regarding the matching of the coil can be found in supplementary materials section.

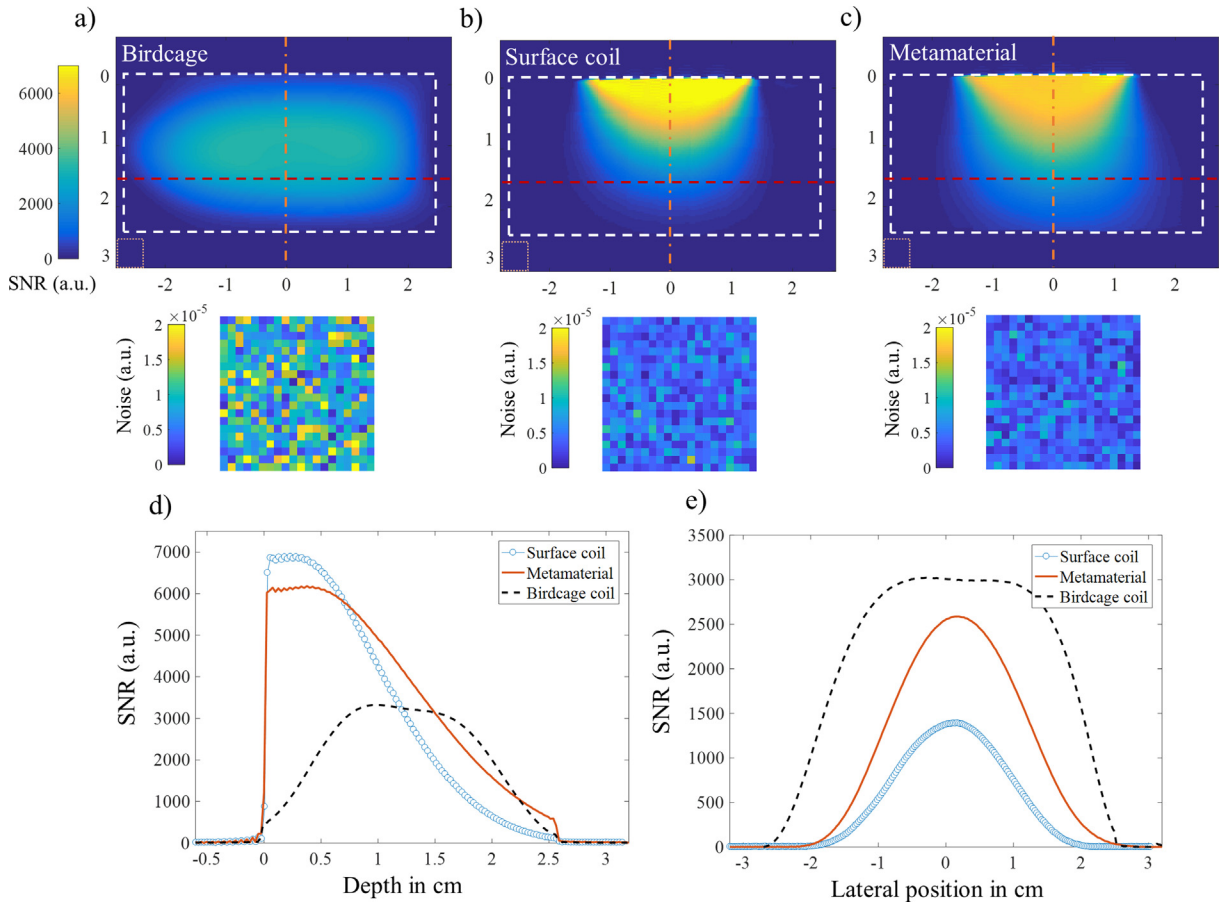

Fig. 5. Measured SNR on the phantom. Median sagittal slices are presented for (a) the birdcage coil, (b) the surface coil alone and (c) the surface coil with the HMA. White dashed boxes denote the position of the phantom. Vertical and horizontal dashed lines depict the position of the profiles shown below. Relative positions are in cm. SNR is given in arbitrary units. The orange dotted square boxes denote the noise region of interest outside of the phantom. Noise signal is shown in each case. (d) SNR profiles as function of depth for the surface coil alone (blue circles), in the presence of the HMA (solid red line) and for the birdcage coil (dashed black line). (e) SNR profiles as function of the lateral position at a depth of 1.65 cm. (For interpretation of the references to colour in this figure legend, the reader is referred to the web version of this article.)

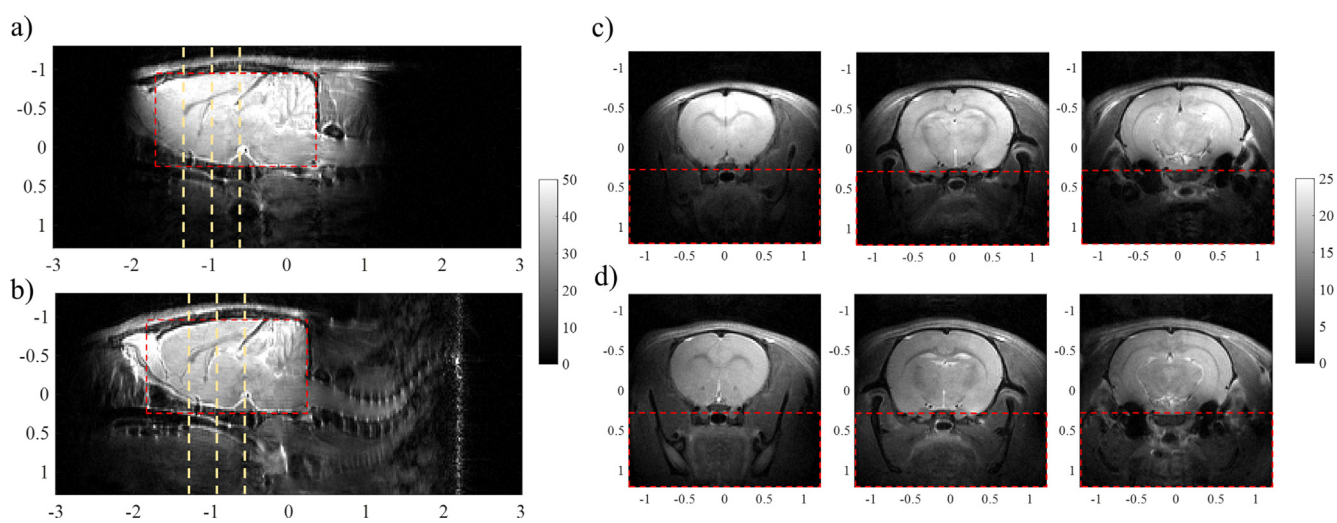

Fig. 6. *In vivo* measurements. Median sagittal slice obtained with the surface coil (a) alone and (b) in presence of the HMA. The artifact on the right hand side of (b) corresponds to the end of the gradient magnetic field. The red dotted boxes denote the brain region of interest. Vertical dashed lines denote the positions of the axial slices shown aside. A set of three axial slices across the rat brain (head to tail) for the surface coil (c) alone and (d) in presence of the HMA. The red dotted boxes denote the in depth region of interest below the brain. Relative positions are in cm. (For interpretation of the references to colour in this figure legend, the reader is referred to the web version of this article.)

Another interesting point to discuss from the simulation results is that the HMA solution performs better than a wider diameter loop. Fig. 1h clearly shows that for a depth of 2.5 cm the HMA approach as implemented here performs better than a 4 cm diameter loop while maintaining higher B_1^+ efficiency in the vicinity of the loop. Additional numerical results regarding the B_1^+ contributions of each pairs of wires are presented in Fig. S2 of the supplementary materials.

In order to explore this concept experimentally an HMA structure was built and compared to a birdcage coil and to the 3 cm diameter surface coil alone. Fig. 3 shows that the measured B_1^+ amplitude is in qualitative agreement with the numerical results. Comparing the relative improvement obtained numerically from Fig. 1e and experimentally in Fig. 4b, we observe that the depth at which the HMA improvement starts is shallower in experiments. Multiple factors are influencing these results. We approximated the distance between the metallic loop of the surface coil and the phantom liquid. The permittivity and conductivity of the phantom was not measured. Finally, we did not take into account ohmic or radiative losses in the loop coil besides the finite conductivity of copper. Although we cannot directly compare these results to the birdcage B_1^+ distribution, it is useful to have a perspective on the transmission efficiency and homogeneity that can be achieved for such an extreme B_0 field with a standard volume coil.

The phantom experiments presented in Fig. 5 confirm the increase of in depth penetration as well as the extension of the sensitive volume along the long axis of the phantom. Unlike in Fig. 4a, we observe an SNR plateau between 0–0.5 cm for the surface coil and 0–0.7 cm in presence of the HMA. This effect comes for the power calibration method. We calibrated the RF power in a 1 mm thick coronal slab in the proximity of the coil which leads to signal saturation where the highest B_1^+ magnitude is achieved near the center of the coil. Meanwhile, the SNR profiles presented in Fig. 5d show a steeper decay than observed in Fig. 4a for the B_1^+ efficiency. This effect is expected as the surface coil is used for transmission and reception. In the low flip angle approximation, this results in an SNR proportional to the square of the B_1^+ magnitude as receive and transmit sensitivities are similar. Another interesting observation is the reduction of the noise standard deviation after the addition of the HMA to the surface coil. This is partially explained by the better quality factor achieved once the HMA was installed (Fig. 2b). It is important to note that this observation depends on the loading of the surface coil. Indeed, as opposed to the phantom study, the noise values observed *in vivo* with the same method were almost identical with and without the HMA.

To conclude, we showed that the HMA approach is perfectly compatible with standard equipment for preclinical research protocols. The extension of the sensitive volume of the surface coil allows to image a large portion of the spinal cord while maintaining 85% of the initial SNR in the brain ROI. We believe that such structures bring a new alternative to the conventional volume coil designs at ultra-high field. The concept of combining HMAs and commercial surface coils may help in the design of future versatile RF coils for preclinical MR applications.

Acknowledgement

This project has received funding from the European Union's Horizon 2020 research and innovation program under grant agreement no 736937.

Appendix A. Supplementary material

Supplementary data associated with this article can be found, in the online version, at https://doi.org/10.1016/j.jmr.2019.106567.

References

[1] C.E. Hayes, W.A. Edelstein, J.F. Schenck, O.M. Mueller, M. Eash, An efficient, highly homogeneous radiofrequency coil for whole-body nmr imaging at 1.5 T, J. Magn. Reson. 63 (1985) (1969) 622–628.
[2] G. Shajan, J. Hoffmann, D.Z. Balla, D.K. Deelchand, K. Scheffler, R. Pohmann, Rat brain MRI at 16.4 T using a capacitively tunable patch antenna in combination with a receive array, NMR Biomed. 25 (2012) 1170–1176.
[3] D. Hoult, The nmr receiver: a description and analysis of design, Prog. Nucl. Magn. Reson. Spectrosc. 12 (1978) 41–77.
[4] K. Ugurbil, M. Garwood, M. Robin Bendall, Amplitude-and frequency-modulated pulses to achieve 90 plane rotations with inhomogeneous b1 fields, J. Magn. Reson. 72 (1987) 177–185.
[5] M. Garwood, Y. Ke, Symmetric pulses to induce arbitrary flip angles with compensation for RF inhomogeneity and resonance offsets, J. Magn. Reson. 94 (1991) (1969) 511–525.
[6] B. Belaroussi, J. Milles, S. Carme, Y.M. Zhu, H. Benoit-Cattin, Intensity non-uniformity correction in MRI: existing methods and their validation, Med. Image Anal. 10 (2006) 234–246.
[7] B. Tomanek, L. Ryner, D.I. Hoult, P. Kozlowski, J.K. Saunders, Dual surface coil with high-b1 homogeneity for deep organ mr imaging, Magn. Reson. Imag. 15 (1997) 1199–1204.
[8] D.O. Brunner, N. De Zanche, J. Fröhlich, J. Paska, K.P. Pruessmann, Travelling-wave nuclear magnetic resonance, Nature 457 (2009) 994.
[9] Q.X. Yang, W. Mao, J. Wang, M.B. Smith, H. Lei, X. Zhang, K. Ugurbil, W. Chen, Manipulation of image intensity distribution at 7.0 t: passive RF shimming and focusing with dielectric materials, J. Magn. Reson. Imag.: Off. J. Int. Soc. Magn. Reson. Med. 24 (2006) 197–202.
[10] M.V. Vaidya, C.M. Deniz, C.M. Collins, D.K. Sodickson, R. Lattanzi, Manipulating transmit and receive sensitivities of radiofrequency surface coils using shielded and unshielded high-permittivity materials, Magn. Reson. Mater. Phys. Biol. Med. (2018) 1–12.
[11] T.P. O'reilly, T. Ruytenberg, A.G. Webb, Modular transmit/receive arrays using very-high permittivity dielectric resonator antennas, Magn. Reson. Med. 79 (2018) 1781–1788.
[12] D.I. Hoult, R. Deslauriers, A high-sensitivity, high-b1 homogeneity probe for quantitation of metabolites, Magn. Reson. Med. 16 (1990) 411–417.
[13] S.B. King, L.N. Ryner, B. Tomanek, J.C. Sharp, I.C. Smith, Mr spectroscopy using multi-ring surface coils, Magn. Reson. Med. 42 (1999) 655–664.
[14] R. Mett, J. Sidabras, J. Hyde, Meta-metallic coils and resonators: methods for high q-value resonant geometries, Rev. Sci. Instrum. 87 (2016), 084703.
[15] R.R. Mett, J.W. Sidabras, J.S. Hyde, MRI surface-coil pair with strong inductive coupling, Rev. Sci. Instrum. 87 (2016), 124704.
[16] C. Jouvaud, R. Abdeddaim, B. Larrat, J. De Rosny, Volume coil based on hybridized resonators for magnetic resonance imaging, Appl. Phys. Lett. 108 (2016), 023503.
[17] M. Dubois, L. Leroi, Z. Raolison, R. Abdeddaim, T. Antonakakis, J. De Rosny, A. Vignaud, P. Sabouroux, E. Georget, B. Larrat, et al., Kerker effect in ultrahigh-field magnetic resonance imaging, Phys. Rev. X 8 (2018), 031083.
[18] E. Motovilova, S.Y. Huang, Hilbert curve-based metasurface to enhance sensitivity of radio frequency coils for 7-T MRI, IEEE Trans. Microwave Theory Techn. (2018).
[19] A. Hurshkainen, A. Nikulin, E. Georget, B. Larrat, D. Berrahou, A.L. Neves, P. Sabouroux, S. Enoch, I. Melchakova, P. Belov, et al., A novel metamaterial-inspired RF-coil for preclinical dual-nuclei MRI, Sci. Rep. 8 (2018) 9190.
[20] M. Zubkov, A.A. Hurshkainen, E.A. Brui, S.B. Glybovski, M.V. Gulyaev, N.V. Anisimov, D.V. Volkov, Y.A. Pirogov, I.V. Melchakova, Small-animal, whole-body imaging with metamaterial-inspired RF coil, NMR Biomed. 31 (2018), e3952.
[21] E. Prodan, C. Radloff, N.J. Halas, P. Nordlander, A hybridization model for the plasmon response of complex nanostructures, Science 302 (2003) 419–422.
[22] S. Baur, S. Sanders, A. Manjavacas, Hybridization of lattice resonances, ACS Nano 12 (2018) 1618–1629.
[23] T.S. Vergara Gomez, M. Dubois, S. Glybovski, B. Larrat, J. de Rosny, C. Rockstuhl, M. Bernard, R. Abdeddaim, S. Enoch, F. Kober, Wireless coils based on resonant and nonresonant coupled-wire structure for small animal multinuclear imaging, NMR Biomed. 32 (2019), e4079.
[24] V.L. Yarnykh, Actual flip-angle imaging in the pulsed steady state: a method for rapid three-dimensional mapping of the transmitted radiofrequency field, Magn. Reson. Med. 57 (2007) 192–200.
[25] K. Nehrke, On the steady-state properties of actual flip angle imaging (AFI), Magn. Reson. Med.: Off. J. Int. Soc. Magn. Reson. Med. 61 (2009) 84–92.
[26] A. Nikulin, J. de Rosny, K. Haliot, B. Larrat, A. Ourir, Opencage radio frequency coil for magnetic resonance imaging, Appl. Phys. Lett. 114 (2019), 053503.
[27] L. Kaufman, D.M. Kramer, L.E. Crooks, D.A. Ortendahl, Measuring signal-to-noise ratios in mr imaging, Radiology 173 (1989) 265–267.
[28] H. Gudbjartsson, S. Patz, The Rician distribution of noisy MRI data, Magn. Reson. Med. 34 (1995) 910–914.
[29] T. O'Reilly, W. Brink, A. Webb, Low-loss high-permittivity blocks improves the signal-to-noise ratio of surface coils at 3 tesla, in: Proceedings of the 26th Annual Meeting of ISMRM, Paris, France, vol. 26, 2018, p. 4303.